BEAM-MATTER INTERACTION AND RADIATION DOSE MEASUREMENTS

Vitali Khachatryan

Content

1. Introduction

A secondary radiation is being produced when a particle accelerator beam interacts with matter (walls, equipment, air, etc.). The motivation for radiation measurements is determined by the needs of radiation safety, accelerator and particle beam physics, as well as by investigations related to materials and life science.. Radiation dose measurements allow monitoring and control of radiation levels. Measurement results provide the basis for construction of radiation protection walls and shields, and for the development of safety procedures. Radiation measurements are useful for the determination of particle accelerator beam parameters. They are based on measurements by tools and detectors of the beam diagnostic system. Combining beam diagnostics results with numerical simulations of particle transport, radiation dose measurements enable one to calculate parameters for irradiation of samples for materials and life science experiments.

Equipment and tools for radiation measurements available at CANDLE include: dosimeter based on Geiger-Muller counter for the measurement of radiation dose due to natural background and for residual dose measurements; a ionization chamber that can cope with high rate radiation and which is suitable for the measurement of prompt radiation produced during accelerator operation; Faraday cups, YAG screen stations, spectrometer and dosimeters.

Experimental tasks include: 1) search for high levels of Radon concentration in the basement rooms applying a high precision Geiger-Muller counter dosimeter; 2) measurements of the dose rates during AREAL accelerator operation by an ionization chamber and study of the radiation attenuation achieved by the protective wall.

The figure depicts a 2D dose distribution in the AREAL accelerator hall simulated by the FLUKA particle transport code.

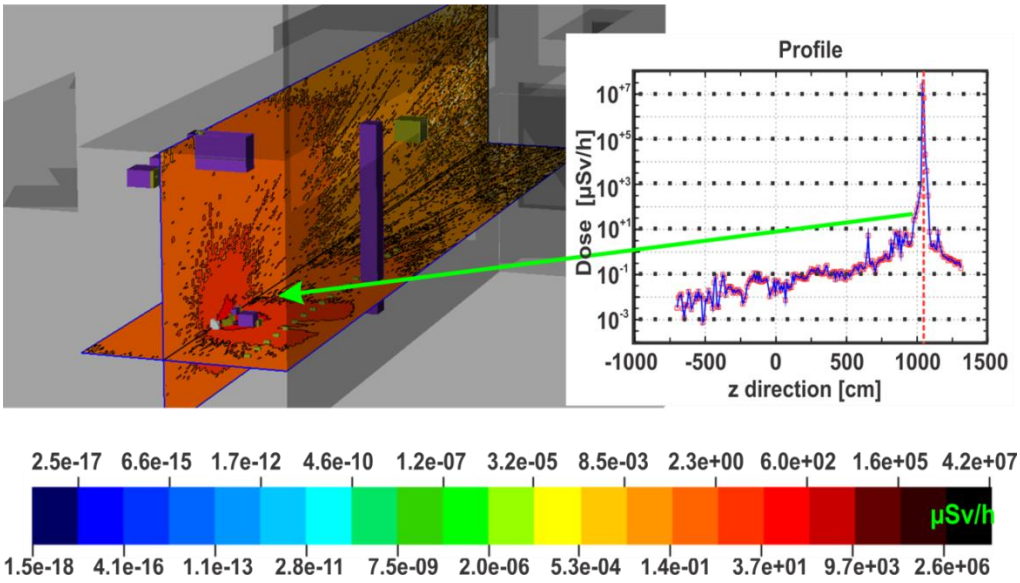

2. Passage of electrons through the matter

2.1 Energy Loss by Electrons

Electrons interact with material through several mechanisms:

Ionization $\mathrm{e}^- + \mathrm{A} \rightarrow \mathrm{e}^- + \mathrm{A}^+ + \mathrm{e}^-$;

Moller scattering $\mathrm{e}^- + \mathrm{e}^- \rightarrow \mathrm{e}^- + \mathrm{e}^-$;

Bremsstrahlung $\mathrm{e}^- + \mathrm{e}^-(\mathrm{A}) \rightarrow \mathrm{e}^-(\mathrm{A}') + \gamma$;

Pair production $\mathrm{e}^- + \mathrm{e}^-(\mathrm{A}) \rightarrow \mathrm{e}^-(\mathrm{A}') + (\mathrm{e}^+ + \mathrm{e}^-)$;

etc.

Electron (positron) scattering is considered as ionization when the energy loss per collision is below $0.255\ MeV$, and as Möller's (Bhabha) scattering when it is above.

At high energies (starting from a few tens of MeVs) bremsstrahlung mechanism prevails.

2.3 Energy loss by ionisation (electron and positron)

In collisions of charged particles with a matter occurring excitation and ionization. Energy loss during bremsstrahlung must also be considered for relativistic particles. Interacting neutral

particles must produce charged particles, which are then detected during their specific interaction processes. For photons these processes are known as Compton scattering, photoelectric effect and pair production of electrons. The electron can be observed through a sensitive ionization detector, which is generated during photon interactions.

Exact calculation taking into account the specific differences between the incident heavy particles and electrons gives a more accurate formula for the loss of electron energy as a result of ionization and excitation [27-Grupen].

$$-\frac{dE}{dx} = 4\,\pi\, N_A r_e^2 m_e c^2 \frac{Z}{A}\cdot\frac{1}{\beta^2}\left(\ln\frac{\gamma m_e c^2 \beta\sqrt{\gamma-1}}{\sqrt{2}I} + \frac{1}{2}(1-\beta^2) - \frac{2\gamma-1}{2\gamma^2}\ln 2 + \frac{1}{16}\left(\frac{\gamma-1}{\gamma}\right)^2\right) \quad (1.1)$$

This expression agrees with the general Bethe–Bloch relation within $10\%-20\%$. The kinematics of electron-electron collisions and screening effects also it takes into account.

The treatment of the ionisation loss of positrons is similar to that of electrons if one considers that these particles are of equal mass, but not identical charge.

For completeness, we also give the ionisation loss of positrons [28- Grupen]:

$$-\frac{dE}{dx} = 4\,\pi\, N_A r_e^2 m_e c^2 \frac{Z}{A}\cdot\frac{1}{\beta^2}\left(\ln\frac{\gamma m_e c^2 \beta\sqrt{\gamma-1}}{\sqrt{2}I} - \frac{\beta^2}{24}\left[23 + \frac{14}{\gamma+1} + \frac{10}{(\gamma+1)^2} + \frac{4}{(\gamma+1)^3}\right]\right) \quad (1.2)$$

Since positrons are antiparticles of electrons, there is, however, an additional consideration: if positrons come to rest, they will annihilate with an electron normally into two photons which are emitted anti-collinearly. Both photons have energies of $511\ keV$ in the centre-of-mass system, corresponding to the rest mass of the electrons. The cross section for annihilation in flight is given by [28- Grupen]

$$\sigma(Z,E) = \frac{Z\pi r_e^2}{\gamma+1}\left[\frac{\gamma^2+4\gamma+1}{\gamma^2-1}\ln\left(\gamma+\sqrt{\gamma^2-1}\right) - \frac{\gamma+3}{\sqrt{\gamma^2-1}}\right] \quad (1.3)$$

More details about the ionisation process of elementary particles, in particular, its spin dependence, can be taken from the books of Rossi and Sitar et al. [1–3- Grupen].

2.4 Energy loses by electron and positron via collision (PDG)

For electrons and positrons, stopping power is different from stopping the power of heavy particles. The difference is kinematics, charge, spin and the characteristics of the electron that causing ionization. A large part of electron's energy transfers to atomic electrons (taken as free), which is described by the Møller cross section. In a single collision the maximum energy transition equals to total kinetic energy $W_{max} = m_e c^2 (\gamma - 1)$, but in case of identical particles, the maximum is half of this at $W_{max}/2$. (The results will be the same if transferred energy equals ϵ or $W_{max} - \epsilon$. The stopping power calculation is done for the faster of the two emerging electrons by convention). In the formula provided below stopping power is the first moment of the Møller cross section [22-PDG] (divided by dx)

$$\left\langle -\frac{\mathrm{dE}}{\mathrm{dx}}\right\rangle = \frac{1}{2}\mathrm{K}\frac{\mathrm{Z}}{\mathrm{A}}\frac{1}{\beta^2}\left[\ln\frac{\mathrm{m_e c^2}\beta^2\gamma^2\{\mathrm{m_e c^2}(\gamma-1)/2\}}{\mathrm{I^2}} + (1-\beta^2) - \frac{2\gamma-1}{\gamma^2}\ln 2 + \frac{1}{8}\left(\frac{\gamma-1}{\gamma}\right)^2 - \delta\right] \quad (1.4)$$

By substituting a logarithmic term in the Bethe equation by $W_{max} = m_e\, c^2(\gamma - 1)/2$ it can be compared with the logarithmic term in the above formula. The two forms differ by $\ln 2$. For describing electron-positron scattering a more complicated cross sectional formula called Bhabha cross section is used [22-PDG]. The identical particle problem doesn't exist in this case so we can consider that $W_{max} = m_e\, c^2\ (\gamma\ -\ 1)$. The first moment of the Bhabha equation results to the following.

$$\left\langle -\frac{dE}{dx} \right\rangle = \frac{1}{2} K \frac{Z}{A} \frac{1}{\beta^2} \left[\ln \frac{m_e c^2 \beta^2 \gamma^2 \{m_e c^2 (\gamma - 1)\}}{2I^2} + 2 \ln 2 - \frac{\beta^2}{12} \left(23 + \frac{14}{\gamma+1} + \frac{10}{(\gamma+1)^2} + \frac{4}{(\gamma+1)^3} \right) - \delta \right] \quad (1.5)$$

Density effect correction δ was added to Uehling's equations [22-PDG] by following ICRU 37 [11-PDG] in both cases.

According to **Figure 1.1** stopping powers for e^-, e^+ and heavy particles do not differ dramatically. In silicon material, the minimum value for e^- is $1.50 MeV\ cm^2/g$ (at $\gamma = 3.3$); for positrons, $1.46 MeV\ cm^2/g$ (at $\gamma = 3.7$), and for μ^- $1.66 MeV\ cm^2/g$ (at $\gamma = 3.58$).

2.5 Radiation Length

High-energy electrons interact with matter, mainly by bremsstrahlung while high-energy photons interact by electron-positron pair production. The characteristic amount of matter, traversed by those particles is called the radiation length X_0 (measured in gram cm^{-2}). The radiation length is the mean distance over which a high-energy electron loses all but $1/e$ of its energy by bremsstrahlung. Equivalently, it is the 7/9 part of the mean free path for pair production by a high-energy photon [41-PDG]. For high-energy electromagnetic cascades, the radiation length is also suitable. In **Eq. (1.6)** it is shown X_0 calculation which is tabulated by Y.S. Tsai [42-PDG]:

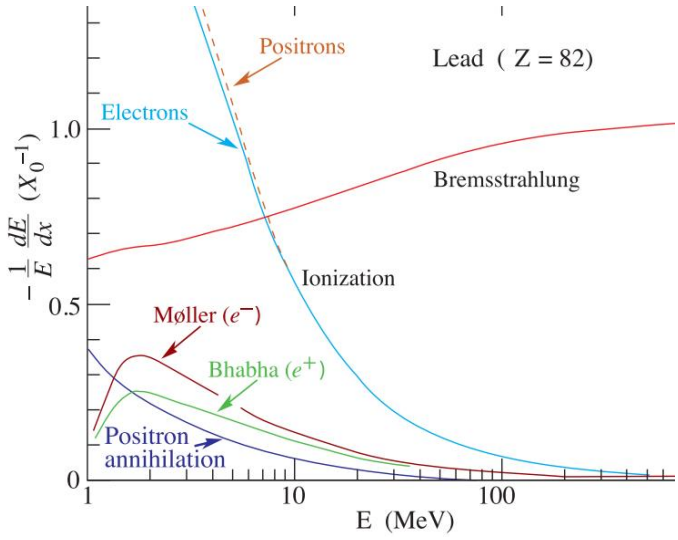

Figure 1.1: Fractional energy loss per radiation length in lead as a function of electron or position energy.

$$\frac{1}{X_0} = 4\alpha r_e^2 \frac{N_A}{N}\{Z^2[L_{rad} - f(Z)] + ZL'_{rad}\} \quad (1.6)$$

For $A = 1\ g\ mol^{-1}$, $4\alpha r_e^2\ N_A/A = (716.408\ g\ cm^{-2})^{-1}$. L_{rad} and L'_{rad} are given in **Table 1.1**. The function $f(Z)$ is an infinite sum. The elements up to uranium can be represented to 4-place accuracy by the following formula

$$f(Z) = a^2[(1 + a^2)^{-1} + 0.20206 - 0.0369a^2 + 0.0083a^4 - 0.002a^6]$$

where $a = \alpha Z$ [43-PDG].

For the mixed compound radiation, the length can be approximated by the following formula $1/X_0 = \sum w_j/X_j$ where w_j and X_j are the fractions by weight and the radiation length for the j-th element.

Although there are accurate formulae to calculate, O. I. Dahl provides a compact fit to the data [19]:

$$X_0 = \frac{716[g-cm^{-2}]A}{Z(Z+1)\ln(287/\sqrt{Z})} \quad (1.7)$$

where A is the atomic mass and Z is the atomic number of the absorber.

Table 1.1. Tsai's L_{rad} and L'_{rad} for use in calculating the radiation length Eq.(1.6)

Element	Z	L_{rad}	L'_{rad}
H	1	5.31	6.144
He	2	4.79	5.621
Li	3	4.74	5.805
Bi	4	4.71	5.924
Others	> 4	$\ln(184.5\ Z^{-1/3})$	$\ln(1194\ Z^{-2/3})$

Results obtained using this formula agree with Tsai's accurate formulae to better than 2.5% for all elements. The radiation associated with the mixture or compound may be approximated by the formula $1/X_0 = \sum w_i/X_{oi}$, where w_i and $X_{oi}$are the fractions by weight and the radiation length for the $i-th$ element.

2.6 Bremsstrahlung

An electron loses energy by bremsstrahlung at a rate nearly proportional to its energy, while the ionization loss rate varies only logarithmically with the electron energy. The critical energy E_c is sometimes defined as the energy at which the two loss rates are equal. The value of the critical energy when bremsstrahlung starts to prevail over ionization mechanism can be obtained by the expressions: $E_c = \frac{610MeV}{Z+1.24}$ for solids and liquids and $E_c = \frac{710MeV}{Z+0.92}$ for the gases.

Alternatively, Rossi [29] defines the critical energy as the energy at which the ionization loss per radiation length is equal to the electron energy. Experimental results prove that Rossi's form of the critical energy definition describes transverse electromagnetic shower development more accurately [20].

Bremsstrahlung radiation is emitted when the fast-moving charged particle is decelerated in the Coulomb field of the atoms. Though radiation takes place mainly due to the field of the nuclei, atomic electrons also contribute to the process. Since the probability of the bremsstrahlung process is proportional to the $1/\mathrm{M}^2$ (M is the mass of the particle), starting from a few tens MeV, bremsstrahlung becomes the dominant process in the interaction of lightest charged particles electrons and positrons with the most materials. Bremsstrahlung process probability increases with the Z^2 (Z is the atomic number).

Bethe-Heitler formula gives the energy loss rate

$$-\frac{\mathrm{dT_e}}{\mathrm{dx}} = \mathrm{n\ T_e\ \alpha\ Z^2 r_e^2}\left(4\ln\frac{183}{\mathrm{z^{1/3}}} + \frac{2}{9}\right) \qquad (1.8)$$

where n is the concentration of the atoms, α is the fine structure constant, $\mathrm{r_e} = \mathrm{e}^2/(\mathrm{m_e c}^2)$ and it is assumed, that the kinetic energy of the electrons $\mathrm{T_e} \gg \mathrm{m_e c}^2/\left(\alpha\ \mathrm{Z}^{1/3}\right)$. This condition ensures consideration of the full screening effect. The electron cloud of the atoms contributes to the bremsstrahlung proportional to Z. Radiation spectrum calculation cannot be accurate without taking into account the co-called LPM effect [19].

The bremsstrahlung spectrum cross section approximation in the "complete screening case" at high energies can be done by the formula [42-PDG]

$$\mathrm{d\sigma/dk} = (1/\mathrm{k})4\alpha\ \mathrm{r_e^2}\ \left\{\left(\frac{4}{3} - \frac{4}{3}\mathrm{y} + \mathrm{y}^2\right)[\mathrm{Z}^2(\mathrm{L_{rad}} - \mathrm{f(Z)} + \mathrm{ZL'_{rad}}]\ + \frac{1}{9}(1-\mathrm{y})(\mathrm{Z}^2+\mathrm{Z})\right\} \qquad (1.9)$$

where $\mathrm{y} = \mathrm{k/E}$ is the part of the electron's energy transferred to the radiated photon. At small y which is the case of "infrared limit" the term on the second line varies from 1.7% (low Z) to 2.5% (high Z) of the total/ If it is neglected and the first line shortened with the definition of $\mathrm{X_0}$ given in **Eq. (1.6)**, we have

$$\frac{\mathrm{d\sigma}}{\mathrm{dk}} = \frac{\mathrm{A}}{\mathrm{R\ N_A\ k}}\left(\frac{4}{3} - \frac{4}{3}\mathrm{y} + \mathrm{y}^2\right) \qquad (1.10)$$

Top curve in Fig. 1.1 shows cross this section (times k). This formula takes place except for the point $y = 1$ and $y = 0$. In $y = 1$ case, screening may become incomplete, and $y = 0$ case, infrared divergence is removed by the interference of bremsstrahlung amplitudes from nearby scattering canters (the LPM effect) [44,45-PDG] and dielectric suppression [46,47-PDG].

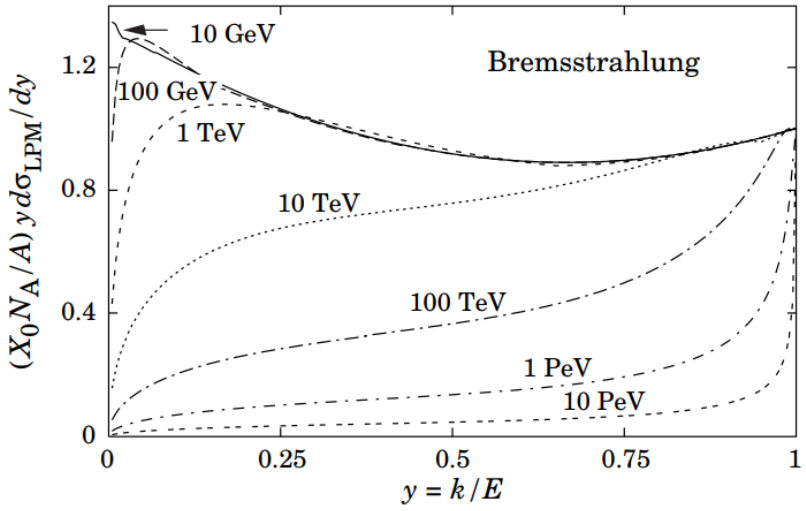

Fig 1.1: Dependence of the normalized bremsstrahlung cross section k $d\sigma_{LPM}/dk$ versus the fractional photon energy $y = k/E$ in lead. The vertical axis's unit containsis photons per radiation length.

One can obtain the expression for the energy loss rate$-\mathrm{dE/dx} = \mathrm{E/X_o}$. Thus, energy loss per unit path length is proportional to the energy of the charged particle and charged particle energy attenuation takes place exponentially:

$$\mathrm{E(x)} = \mathrm{E(0)}\exp(-\mathrm{x/X_0}) \qquad (1.11)$$

The number of photons with energies between $\mathrm{k_1}$and $\mathrm{k_2}$radiated by an electron traveling a distance $\mathrm{d} \ll \mathrm{X_0}$ is

$$\mathrm{N_\gamma} = \frac{\mathrm{d}}{\mathrm{X_0}}\left[\frac{4}{3}\ln\left(\frac{\mathrm{k_2}}{\mathrm{k_1}}\right) - \frac{4\,(\mathrm{k_2}-\mathrm{k_1})}{3\,\mathrm{E_e}} + \frac{\mathrm{k_2^2}-\mathrm{k_1^2}}{2\mathrm{E_e^2}}\right] \qquad (1.12)$$

The mean value of the photon emission in the bremsstrahlung process does not depend on the photon energy. It can be found from the formula

$$\bar{\vartheta} = \frac{\mathrm{m_e c^2}}{\mathrm{E_e}} \qquad (1.13)$$

2.7. Energy loss by photons:

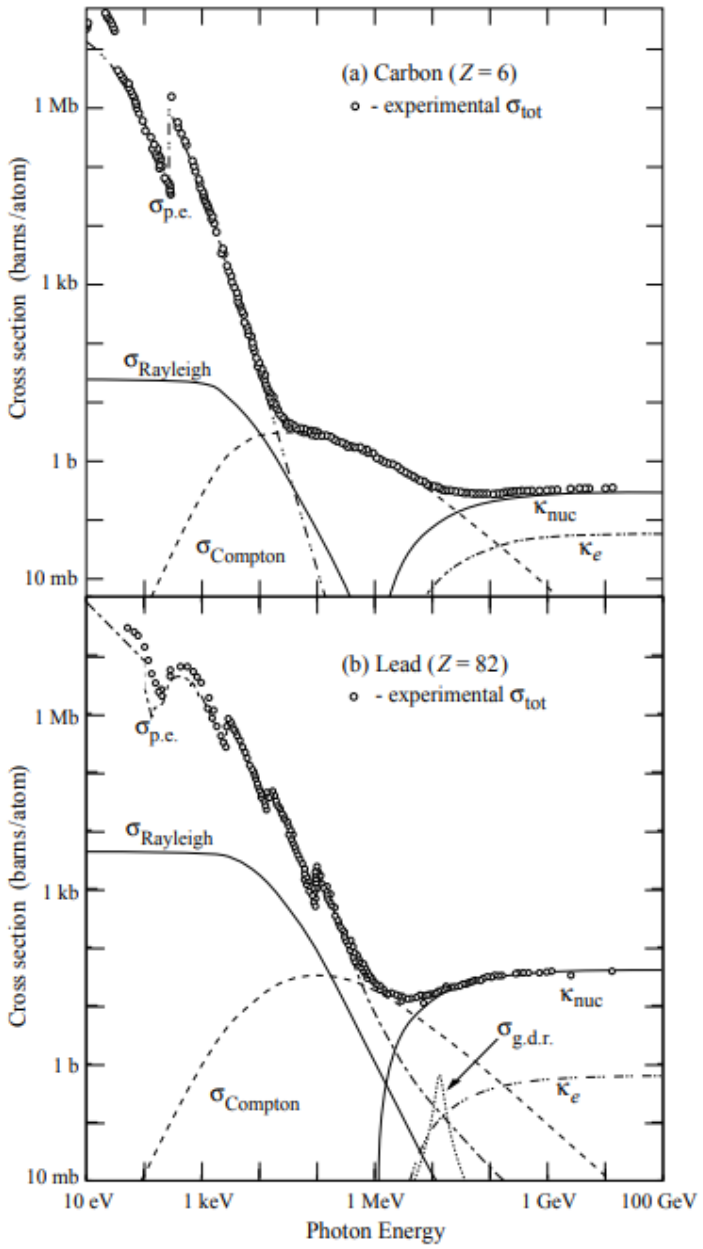

Figure 33.15: Photon total cross sections as a function of energy in carbon and lead with contributions of different processes :

$\sigma_{p.e.}$ = Atomic photoelectric effect on atom

$\sigma_{Rayleigh}$ = Rayleigh (coherent) scattering–atom neither ionized nor excited

$\sigma_{Compton}$ = Incoherent scattering (Compton scattering on electron)

κ_{nuc} = Pair production in nuclear field

κ_e = Pair production, electron field

$\sigma_{g.d.r.}$ = Photonuclear interactions via Giant Dipole Resonance mechanism

Contributions to the photon cross section in a light element (carbon) and a heavy element (lead) are shown in **Fig. 33.15**. At low energies it is seen that the photoelectric effect dominates, although Compton scattering, Rayleigh scattering, and photonuclear absorption also contribute. The photoelectric cross section is characterized by discontinuities (absorption edges) as thresholds for photoionization of various atomic levels are reached. Photon attenuation lengths for a variety of elements are shown in **Fig. 33.16**, and data for $30\ eV < k < 100\ GeV$ for all elements are available from the web pages given in the caption. Here k is the photon energy.

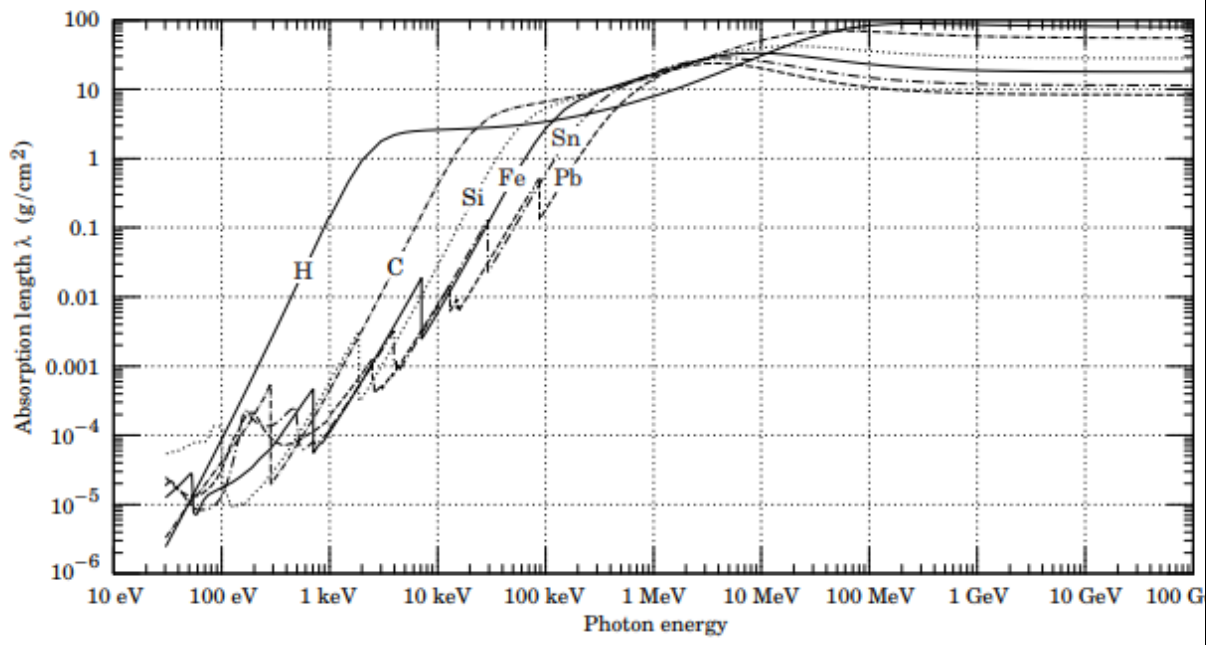

Figure 33.16: The photon mass attenuation length (or mean free path) $\lambda = 1/(\mu/\rho)$ for various elemental absorbers as a function of photon energy. The mass attenuation coefficient is μ/ρ, where ρ is the density. The intensity I remaining after traversal of thickness t (in mass/unit area) is given by $I = I_0\ exp(-t/\lambda)$. The accuracy is a few percent. For a chemical compound or mixture, $1/\lambda_{eff} \approx \Sigma_{elements} w_z/\lambda_z$, where w_Z is the proportion by weight of the element with atomic number Z.

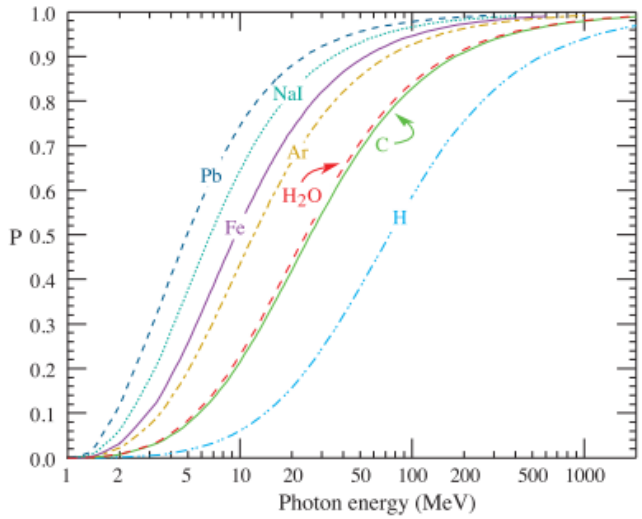

Figure 33.17: Probability P that a photon interaction will result in conversion to an e^+e^- pair. Except for a few-percent contribution from photonuclear absorption around 10 or 20 MeV, essentially all other interactions in this energy range result in Compton scattering off an atomic electron. For a photon attenuation length λ (**Fig. 33.16**), the probability that a given photon will produce an electron pair (without first Compton scattering) in thickness t of absorber is

$P[1 - exp(-t/\lambda)]$.

The increasing domination of pair production as the energy increases is shown in **Fig. 33.17**. Using approximations, Tsai's formula for the differential cross section reduces to

$$\frac{d\sigma}{dx} = \frac{A}{X_0 N_A}\left[1 - \frac{4}{3}x(1-x)\right] \qquad (33.32)$$

in the complete-screening limit valid at high energies. Here $x = E/k$ is the fractional energy transfer to the pair-produced electron (or positron), and k is the incident photon energy.

2.8 Electromagnetic Cascade

When thick absorber is hit by high-energy electron or photon it initiates an electromagnetic cascade as pair production and more electrons and photons with lower energy are generated by bremsstrahlung. The cascade evolution in the longitudinal direction is governed by the high-energy particles and therefore scales as the radiation length in the material. Electrons' energy decreases and falls below the critical energy, and later dissipates it by ionization and excitation rather than by the generation of more shower particles. When describing electromagnetic showers behavior it is convenient to bring up the scale variables $t = x / X_0$; $y = E / E_c$. With

this convention, distance is measured in units of radiation length and energy in units of critical energy.

In Fig. 1.2, longitudinal profiles are shown from the simulation of a 30 GeV electron-induced cascade in iron by EGS4 [56-PDG]. The number of secondary particles which are crossing a plane (very close to Rossi's Π function [2-PDG]) is depends very sensitively on the cutoff energy, here chosen as the a total energy of $1.5\ MeV$ for both e^- and e^+. The number of electrons decreases more drastically than energy deposition. This happens because when increasing the depth at a larger portion of the cascade the energy is carried by photons. Calorimeter measurement depends on the device characteristics, but however, it is not likely to be exactly any of the profiles shown in **Figure 1.1**. In case of gas- based counters, it may be very close to the electron number, but in case of glass- based "Cherenkov" detectors, which have "thick" sensitive regions, it is closer to the energy deposition (total track length). In "Cherenkov" detectors, the detectors the signal is proportional to the "detectable" track length T_d which is in usually less than the total track length T. Real devices are sensitive to particles with energy higher than some threshold E_d, and $T_d = T\ F(E_d/E_c)$. An analytic formula for $F(E_d/E_c)$ is obtained by Rossi [2-PDG] is given by Fabjan in [57-PDG]; see also Amaldi [58-PDG].

The energy deposition mean longitudinal profile in an electromagnetic cascade is described in details by a gamma distribution [59-PDG]:

$$\frac{dE}{dt} = E_0 b \frac{(bt)^{a-1} e^{-bt}}{\Gamma(a)} \qquad (1.14)$$

The maximum t_{max} occurs at $(a - 1)/b$. Fits to shower profiles in elements ranging from carbon to uranium, at energies from $1\ GeV$ to $100\ GeV$. The energy deposition profiles are well described by **Eq. (1.14)** with

$$t_{max} = (a-1)/b = 1.0 \times (\ln y + C_j)\,, \quad j = e, \gamma \qquad (1.15)$$

where $C_e = -0.5$ for electron-induced cascades and $C_\gamma = +0.5$ for photon-induced cascades. To use **Eq. (1.14)**, one finds $(a - 1)/b$ from Eq. (1.15), then finds a either by assuming $b \approx 0.5$ or by finding a more accurate value from **Figure 1.3**.

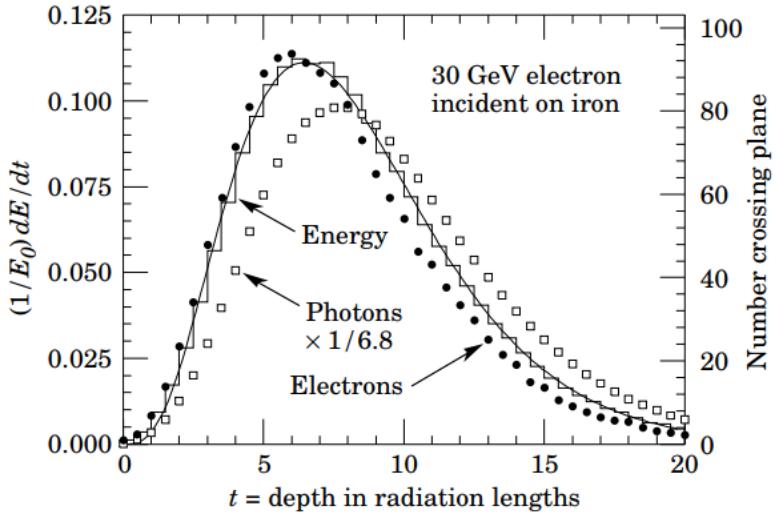

Figure 1.2: 30 GeV electron-induced cascade simulation in iron. Fractional energy deposition per radiation length is shown by the histogram, and the curve is a gamma-function fit to the distribution.

The results are identical for the electron number profiles, but it depends on the atomic number of the medium. The same form for the electron number maximum was obtained by Rossi in the assumption, but with $C_e = -1.0$ and $C_\gamma = -0.5$; we regard this as superseded by the EGS4 result.

Parameterization of "shower length" $X_s = X_0/b$ is done less conveniently, since b depends upon both Z and incident energy, as shown in **Figure 1.3**. As a consequence of this Z dependence, the number of electrons that are crossing a plane near shower maximum is underestimated using the approximation of Rossi for carbon and significantly overestimated for uranium. Necessarily the same b values are obtained for incident e^- and e^+. For most cases, it is sufficient to take $b \approx 0.5$.

Ultra-high energy photons and electrons have a greater length of showers than at lower energies since the first or first few interaction lengths are increased via the mechanisms described above.

Near the origin, the EGS4 cascade (or a real cascade) increases more sharply, whereas the gamma function distribution is very flat. As a result (**Eq. 1.14**) fails abominably. For the first two radiation lengths cases; it was necessary to remove this region in making fits.

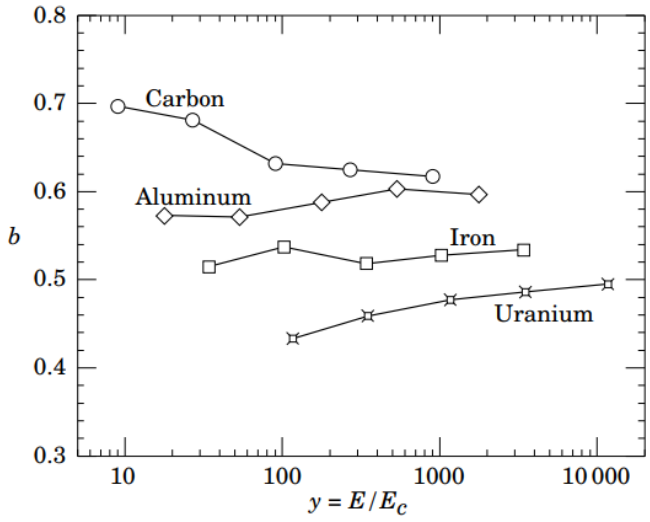

Figure 1.3: Scale factor b fit values for energy deposition profiles for a variety of elements for incident electrons with $1 \leq E_0 \leq 100\ GeV$.

Since fluctuations play an important role, (**Eq.1.14**) should be used only in applications where mean behavior is adequate. Fast simulation algorithms were developed by Grindhammer et al. in which the fluctuation and correlation of a and b are obtained by fitting (**Eq. 1.14**) to individually simulated cascades. Then from the correlated distributions [60-PDG] generated profiles for cascades using a and b were chosen.

The development of electromagnetic showers in the transverse direction in different materials scales quite accurately with the Moliere radius R_M, given by [61,62-PDG] $R_M = X_0\ E_s\ /\ E_c$, where $E_s \approx 21\ MeV$, and the Rossi definition of E_c is used.

In a material with weight fraction w_j of the element, with radiation length X_j and critical energy E_{cj}, the Moliere radius is expressed by

$$\frac{1}{R_M} = \frac{1}{E_s}\sum\frac{w_j E_{cj}}{X_j} \qquad (1.16)$$

Lateral distribution measurements in electromagnetic cascades are depicted in [61, 62-PDG]. On the average, only 10% of the energy falls outside the cylinder with radius R_M. About 99% falls inside of $3.5R_M$, but at this radius and beyond composition effects play an important role and the scaling with R_M fails. The distributions are represented by a narrow core, and broaden as the shower develops. They are often represented as the sum of two Gaussians, and Grindhammer [60-PDG] definses them with the function

$$f(r) = \frac{2rR^2}{(r^2+R^2)^2} \qquad (1.17)$$

where R is a phenomenological function of x/X_0 and $\ln E$. The LPM effect reduces the cross sections for bremsstrahlung and pair production at high energies and hence can cause significant elongation of electromagnetic cascades [45-PDG].

3. Environmental radioactivity

3.1 Environmental radioactivity: The long-lived natural radio-nuclides K^{40}, Th^{232}, and U^{238} with average abundances of 1.6, 11.1 and $2.7\,ppm$ (corresponding to $412, 45$ and $33\,Bq/kg$, respectively) in the earth's crust have large local variations. In most cases, γ radiation emitted due to the decay of natural radioactivity and its unstable daughters constitutes the dominant share in the local radiation field. Typical low-background applications require levels of natural radioactivity on the order of ppb or ppt in the detector components. Passive or active shielding is used to suppress external γ radiation down to an equivalent level. **Fig. 35.10** shows the energy-dependent attenuation length $\lambda(E_\gamma)$ as a function of γ-ray energy E_γ for three common shielding materials (water, copper, lead). The thickness ℓ required to reduce the external flux by a factor $f > 1$ is estimated, assuming exponential damping:

$$\ell = \lambda(E_\gamma) \cdot \ln f$$

At $100\,keV$, a typical energy scale for dark matter searches (or $2.615\,MeV$, for a typical double-beta decay experiment), attenuation by a factor $f = 105$ requires $67(269)\,cm$ of H_2O, $2.8(34)\,cm$ of Cu, or $0.18(23)\,cm$ of Pb. Such estimates allow for an order-of-magnitude determination of the experiment dimensions.

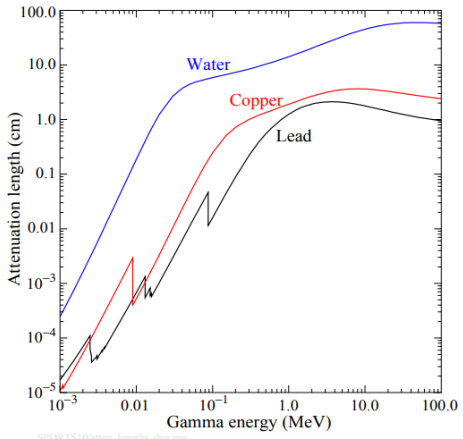

Figure 35.10: γ-ray attenuation lengths in some common shielding materials. The mass attenuation data has been taken from the NIST data base XCOM (*pdg.lbl.gov*).

A precise estimation of the magnitude of the external gamma-ray background, including scattering and the effect of analysis-energy cuts, requires Monte Carlo simulations based on the knowledge of the radioactivity field present in the laboratory. Detailed modeling of the γ-ray flux in a large laboratory, or inside the hermetic shielding, needs to cope with a very small probability of generating any signal in the detector. It is often advantageous to calculate solid angle of the detector to the background sources and mass attenuation of the radiation shield separately, or to employ importance sampling. The former method can lead to loss of energy-direction correlations while in the latter has to balance CPU-time consumption against the loss of statistical independence. These approaches reduce the computation time required for a statistically meaningful number of detector hits to manageable levels.

Water is commonly used as shielding medium for large detectors, as it can be obtained cheaply and purified effectively in large quantity. Water purification technology is commercially available. Ultra-pure water, instrumented with photomultiplier tubes, can serve as active cosmic-ray veto counter. Water is also an effective neutron moderator and shield. In more recent underground experiments that involve detectors operating at cryogenic temperature, liquefied gases (e.g. argon) are being used for shielding as well.

3.2 Radioactive impurities in detector and shielding components: After suppressing the effect of external radioactivity, radioactive impurities, contained in the detector components or attached to their surfaces, become important. Every material contains radioactivity at some level. The activity can be natural, cosmogenic, man-made, or a combination of them. The determination of the activity content of a specific material or component requires case-by-case analyses, and is rarely obtainable from the manufacturer. However, there are some general rules that can be used to guide the pre-selection. For detectors designed to look for electrons (for example in double-beta decay searches or neutrino detection via inverse beta decay or elastic scattering), intrinsic radioactivity is often the principal source of background. For devices detecting nuclear recoils (for example in dark matter searches), this is often of secondary importance as ionization signals can be actively discriminated on an event-by-event basis. Decay induced nuclear reactions become a concern.

For natural radioactivity, a rule of thumb is that synthetic substances are cleaner than natural materials. Typically, more highly processed materials have lower activity content than raw substances. Substances with high electro-negativity tend to be cleaner as the refining process preferentially removes K, Th, and U. For example, Al is often found to contain considerable amounts of Th and U, while electrolytic Cu is very low in primordial activities. Plastics or liquid hydrocarbons, having been refined by distillation, are often quite radiopure. Tabulated radioassay results for a wide range of materials can be found in Refs. [103] and [104]. Radioassay results from previous underground physics experiments are being archived at an online database [105].

The long-lived U^{238} daughter Pb^{210} ($T_{1/2} = 22.3\ y$) is found in all shielding lead, and is a background concern at low energies. This is due to the relatively high endpoint energy ($Q_\beta = 1.162\ MeV$) of its beta-unstable daughter Bi^{210}. Lead refined from selected low-U ores have specific activities of about $5-30\ Bq/kg$. For applications that require lower specific activity, ancient lead (for example from Roman ships) is sometimes used. Because the ore processing and lead refining removed most of the U^{238}, the Pb^{210} decayed during the long waiting time to the level supported by the U-content of the refined lead. Lining the lead with copper to range out the low-energy radiation is another remedy. However, intermediate-Z materials carry additional cosmogenic-activation risks when handled above ground, as will be discussed below. Pb^{210} is also found in solders.

Man-made radioactivity, released during above-ground nuclear testing and nuclear power production, is a source of background. The fission product Cs^{137} can often be found attached to the surface of materials. The radioactive noble gas Kr^{85}, released into the atmosphere by nuclear reactors and nuclear fuel re-processing, is sometimes a background

concern, especially due to its high solubility in organic materials. Post-World War II steel typically contains a few tens of mBq/kg of Co^{60}.

Surface activity is not a material property per se but is added during manufacturing and handling. Surface contamination can often be effectively removed by clean machining, etching, or a combination of both. The assembly of low-background detectors is often performed in controlled enclosures (e.g. clean rooms or glove boxes) to avoid contaminating surfaces with environmental substances, such as dust, containing radioactivity at much higher concentrations than the detector components. Surfaces are cleaned with high purity chemicals and de-ionized water. When not being processed components are best stored in sealed bags to limit dust deposition on the surface, even inside clean rooms. Surface contamination can be quantified by means of wipe-testing with acid or alcohol wetted Whatman 41 filters. Pre-soaking of the filters in clean acid reduces the amount of Th and U contained in the paper and boosts analysis sensitivity. The paper filters are ashed after wiping and the residue is digested in acid. Subsequent analysis by means of mass spectroscopy or neutron activation analysis is capable of detecting less than $1\ pg/cm^2$ of Th and U.

The most demanding low-rate experiments require screening of all components, which can be a time consuming task. The requirements for activity characterization depend on the experiment and the location and amount of a particular component. Monte Carlo simulations are used to quantify these requirements. Sensitivities of the order $\mu Bq/kg$ or less are sometimes required for the most critical detector components. At such a level of sensitivity, the characterization becomes a challenging problem in itself. Low-background α, β, and γ-ray counting, mass spectroscopy, and neutron activation analysis are the commonly used diagnostic techniques.

3.3 Radon and environmental radioactivity: The noble gas Rn^{222}, a pure α-emitter, is a U^{238} decay product. Due to its relatively long half-life of $3.8\ d$ it is released by surface soil and is found in the atmosphere everywhere. Rn^{220} (Th^{232} decay product) is mostly unimportant for most low-background experiments because of its short half-life. The Rn^{222} activity in air ranges from $10\ to\ 100\ mBq/L$ outdoors and 100 to thousands of mBq/L indoors. The natural radon concentration depends on the weather and shows daily and seasonal variations. Radon levels are lowest above the oceans. For electron detectors, it is not the Rn itself that creates background, but its progeny Pb^{214}, Bi^{214}, Bi^{210}, which emit energetic beta and γ radiation. Thus, not only the detector itself has to be separated from contact with air, but also internal voids in the shield which contain air can be a background concern. Radon is quite soluble in water and even more so in organic solvents. For large liquid scintillation detectors, radon mobility due to convection and diffusion is a concern. To define a scale: typical double-beta-decay searches are restricted to $< \mu Bq/kg_{\text{detector}}$ (or 1 decay per $kg_{detector}$ and per 11.6 days) activities of Rn^{222} in the active medium. This corresponds to a steady-state population of $0.5\ atoms/kg_{detector}$ or $50\ \mu L/kg_{detector}$ of air (assuming $20\ mBq/L$ of radon in the air). The demand on leak tightness can thus be quite demanding. The decay of Rn itself is a concern for some recoil type detectors, as nuclear recoil energies in α decays are substantial ($76\ keV$ in the case of Rn^{222}).

Low-background detectors are often kept sealed from the air and continuously flushed with boil-off nitrogen, which contains only small amounts of Rn. For the most demanding

applications, the nitrogen is purified by multiple distillations, or by using pressure swing adsorption chromatography. Then only the Rn outgassing of the piping (due to its intrinsic U content) determines the radon concentration. Radon diffuses readily through thin plastic barriers. If the detector is to be isolated from its environment by means of a membrane, the choice of material is important [106].

Prolonged exposure of detector components or raw materials to air leads to the accumulation of the long-lived radon daughter Pb^{210} on surfaces. Due to its low Q-value of $63.5\,keV$, Pb^{210} itself is only a problem when extreme low energy response is important. However, because of its higher Q-value, the lead daughter Bi^{210}, is a concern up to the MeV scale. The alpha unstable Bi-daughter Po^{210} ($E_\alpha = 5304\,keV$) contributes not only to the alpha background but can also induce the emission of energetic neutrons via (α, n) reactions on low-Z materials (such as $F, C, Si \ldots etc$). The neutrons, in turn, may capture on other detector components, creating energetic background. The (α, n) reaction yield induced by the α decay of Po^{210} is typically small ($6 \cdot 10^{-6}\, n/\alpha$ in Teflon, for example). Some data is available on the deposition of radon daughters from air onto materials, see e.g. [108]. This data indicates effective radon daughter collection distances of a few cm in air. These considerations limit the allowable air exposure time. In case raw materials (e.g. in the form of granules) were exposed to air at the production site, the bulk of the finished detector components may be loaded with Pb^{210} and its daughters. These are difficult to detect as no energetic gamma radiation is emitted in their decays. Careful air-exposure management is the only way to reduce this source of background. This can be achieved by storing the parts under a protective low-radon cover gas or keeping them sealed from radon.

State-of-the-art detectors can detect radon even at the level of few atoms. Solid state, scintillation, or gas detectors utilize alpha spectroscopy or are exploiting the fast $\beta - \alpha$ decay sequences of Bi^{214} and Po^{214}. The efficiency of these devices is sometimes boosted by electrostatic collection of charged radon from a large gas volume into a small detector.

Radon (a radioactive noble gas, originating from the soil's uranium and thorium content) is considered responsible for more than half the average natural radiation dose for humans and one of the major causes of lung cancer. The health concerns of radon made regulatory control necessary and many countries implemented some measures for handling exposure to radon. The usual regulatory approach is specifying dose limits, an amount of radiation dose that is acceptable, these would be translated to reference levels, meaning permissible activity concentrations in various media (set in a way not to reach the dose limits). These reference levels then would be compared to the measured activity concentrations and if those concentrations exceed the reference levels the appropriate measures set in the national regulations would have to be implemented. Developments in the dose conversion calculations further raised the importance of radon (the conversion factors were approximately tripled from the previously used ICRP 65). The European Union has included exposure to radon in the 2014 Basic Safety Standards, which requires the Member States to introduce reference levels for indoor radon concentrations not exceeding (as an annual average) 200 Bq m−3 for new dwellings and new buildings with public access, 300 Bq m−3 for existing dwellings, and 300 Bq m−3 for existing buildings with public access, allowing for low occupancy time a maximum of 1000 Bq m−3. Since regulating radon concentrations requires a large number of measurements some method is necessary to optimize

the allocation of the limited resources available for each country. The indoor radon concentration and the exposure from radon are dependent on many factors, but an assumption can be made that geology is a major control on the variation of indoor radon. This radon potential can be described by many different ways.

Geogenic radon potential concepts The EU BSS describes radon-prone areas as a geographic area or administrative region where surveys indicate that the percentage of dwellings expected to exceed national reference levels is significantly higher than in other parts of the country (Bossew 2015). This is a good concept for national regulations, however it can't be used across borders, it is highly dependent on national regulations and gives only a sense of risk related to the average concentration of the particular country, as high or as low it may be. One of the often (Gruber et al. 2013, Szabó et al. 2014, Bossew 2015, Pásztor et al. 2016) used methods assessing the geogenic radon potential is the continuous variable originally proposed by Neznal et al. 2004. , where GRP is the geogenic radon potential, c∞ is the equilibrium soil gas radon activity concentration at a definite depth (0.8–1 m) (kBq m −3) and k is the soil gas permeability (m2). Based on research conducted in the Czech Republic, three categories of GRP were set: low (GRP < 10), medium (10 < GRP < 35) and high (35 < GRP) (Szabó et al. 2014). In practice there are some variations on providing the values for c and k (Gruber et al. 2013). If C and k values are not available, then the radon potential is usually estimated from proxies. Such proxies are the standardised indoor radon concentration (measured in defined standard conditions such as ground floor rooms, presence of a basement, etc. to 'factorise out' anthropogenic factors) The standardised indoor radon concentration is correlated to the GRP, with inaccuracies caused by remaining unaccounted for or poorly assessed factors. Other quantities such as equivalent uranium (eU) or dose rate have similarly describable relations to the GRP, however these relations can be locally different, according to the regional predominance of some factors. The controlling factors have to be taken into account when using substitutes for the soil radon in the formula (Gruber et al. 2013). A different way of defining radon potential is based on multivariate cross-tabulation. This method results in an index with a categorical-ordinal quantity, the results are given in classes such as (I, II, III, IV) or (low, medium, high). Classes are assigned based on scores either assigned to a combination of input quantities or calculated as the sum of points delegated to the input quantities. The second type allows for the consideration of multiple factors. Available quantities are soil radon, permeability, standardised indoor concentration, equivalent uranium concentration or other geochemical quantities, external terrestrial gamma dose rate, geological categories, quantities related to tectonics, and the presence of 'special features' like mines, caves, water bodies and other extraordinary conditions, which are coded binary (yes, no) (Gruber et al. 2013). For compiling maps, similarly to the definition, several options exist. First the definition of the target variable has to be decided upon. Then the mentioned variable has to be matched to spatial units (area), which will serve as the basis of the map. These spatial units can take various shapes and forms such as administrative or geological units or a grid cells. Geographical units might be a practical choice for the radon potential, and if desired those units can be decompiled into a grid system. The spatial units are then assigned a value derived from the measured target variables inside (arithmetic mean, geometric mean, median, etc.) (Gruber et al. 2013). If insufficient data is available for the mean calculation to be representative of the area that technique shouldn't be used. Various estimation or interpolation

techniques (local regression methods, disjunctive kriging, Bayesian inference or extensive Monte Carlo simulations) can be implemented during the construction of such maps, but it should be kept in mind that the interpolated concentration is only an estimate, not the actual radon concentration, even though it can be useful for the visualisation of the data and in defining areas with higher risk probability (Cafaro et al. 2014). The different spatial units offer different advantages and disadvantages. Administrative boundaries make administrative action easier, but disregard the relation between the radon potential and the geology and soil properties. Grids makes mapping independent from other variables, but ignores variation within the grid cells. Geological boundaries are much more closely related to the radon potential but still there can be variations in the radon potential inside the geological units (Ielsch et al. 2010). In case of sufficient data density maps can be made by displaying each point of data, without interpolation for the areas between the data points, which would still give an instinctive grasp of the overall situation (McKinley 2015).

3.4 Cosmic rays : Cosmic radiation is a source of background for just about any non-accelerator experiment. Primary cosmic rays are about 90% protons, 9% alpha particles, and the rest heavier nuclei. They are totally attenuated within the first the first few hg/cm^2 of atmospheric thickness. At sea level secondary particles ($\pi^{\pm} : p : e^{\pm} : n : \mu^{\pm}$) are observed with relative intensities $1 : 13 : 340 : 480 : 1420.$

All but the muon and the neutron components are readily absorbed by overburden such as building ceilings and passive shielding. Only if there is very little overburden ($\lesssim 10\ g/cm^2$ or so $[100]$) do pions and protons need to be considered when estimating the production rate of cosmogenic radioactivity.

Sensitive experiments are thus operated deep underground where essentially only muons can penetrate. The muon intensity falls off rapidly with depth. Active detection systems, capable of tagging events correlated in time with cosmic-ray activity, are needed, depending on the overburden. The muonic background is related to low-radioactivity techniques insofar as photonuclear interactions with atomic nuclei can produce long-lived radioactivity directly or indirectly via the creation of neutrons. This happens at any overburden, however, at strongly depth dependent rates. Muon bremsstrahlung, created in high-Z shielding materials, contributes to the low energy background too. Active muon detection systems are effective in reducing this background, but only for activities with sufficiently short half-lives, allowing vetoing with reasonable detector dead time.

Cosmogenic activation of detector components at the surface can be an issue for low-background experiments. Proper management of parts and materials above ground during manufacturing and detector assembly minimizes the accumulation of long-lived activity. Cosmogenic activation is most important for intermediate-Z materials such as Cu and Fe. For the most demanding applications, metals are stored and transported under sufficient shielding to stop the hadronic component of the cosmic rays. Parts can be stored underground for long periods before being used. Underground machine shops are sometimes used to limit the duration of exposure at the surface. Some experiments are even electro-forming copper underground.

3.4 Neutrons: Neutrons contribute to the background of low-energy experiments in different ways: directly through nuclear recoil in the detector medium, and indirectly, through the production of radio-nuclides, capture γs and inelastic scattering inside the detector and its components. The indirect mechanisms allow even remote materials to contribute to the background by means of penetrating γ radiation. Neutrons are thus an important source of low-energy background. They are produced in different ways:

1. At the earth's surface the flux of cosmic-ray secondary neutrons is exceeded only by that of muons;
2. Energetic tertiary neutrons are produced by cosmic-ray muons by nuclear spallation in the detector and laboratory walls;
3. In high-Z materials, often used in radiation shields, nuclear capture of negative muons results in the emission of neutrons;
4. Natural radioactivity has a neutron component through spontaneous fission and (α, n)-reactions.

A calculation with the hadronic simulation code FLUKA [107], using the known energy distribution of secondary neutrons at the earth's surface [110], yields a mass attenuation of $1.5\ hg/cm^2$ in concrete for secondary neutrons. In case energy-dependent neutron-capture cross sections are known, such calculations can be used to obtain the production rate of particular radio-nuclides.

At an overburden of only few meters water equivalent, neutron production by muons becomes the dominant mechanism. Neutron production rates are high in high-Z shielding materials. A high-Z radiation shield, discussed earlier as being effective in reducing background due to external radioactivity, thus acts as a source for cosmogenic tertiary high-energy neutrons. Depending on the overburden and the radioactivity content of the laboratory, there is an optimal shielding thickness. Water shields, although bulky, are an attractive alternative due to their low neutron production yield and self-shielding.

Shields made from plastic or water are commonly used to reduce the neutron flux. The shield is sometimes doped with a substance having a high thermal neutron capture cross section (such as boron) to absorb thermal neutrons more quickly. The hydrogen, contained in these shields, serves as a target for elastic scattering, and is effective in reducing the neutron energy. Neutrons from natural radioactivity have relatively low energies and can be effectively suppressed by a neutron shield. Ideally, such a neutron shield should be inside the lead to be effective for tertiary neutrons. However, this is rarely done as it increases the neutron production target (in form of the passive shield), and the costs increase as the cube of the linear dimensions. An active cosmic-ray veto is an effective solution, correlating a neutron with its parent muon. This solution works best if the veto system is as far away from the detector as feasible (outside the radiation shield) in order to correlate as many background-producing muons with neutrons as possible. The vetoed time after a muon hit needs to be sufficiently long to assure muon bremsstrahlung and neutron-induced backgrounds are sufficiently suppressed. An upper limit to the allowable veto period is given by the veto-induced deadtime, which is related to the muon hit rate on the veto detector. This consideration also constitutes the limiting factor for the physical size of the veto system (besides the cost). The background caused by neutron-induced

radioactivity with live-times exceeding the veto time cannot be addressed in this way. Moving the detector deep underground, and thus reducing the muon flux, is the only technique that addresses all sources of cosmogenic the neutron background.

5. Radiation Dose Measurements at AREAL

ITRODUCTION

Strong motivation for radiation measurement determined by needs of radiation safety, accelerator and beam physics as well material science and life science radiation related investigations.
Radiation dose measurements allow monitoring and control radiation levels.
Radiation dose measurement results provide basis for construction radiation protection walls and shields and development of safety procedures.
Radiation dose measurement can be useful for the beam parameter determination along with measurements by tools and detectors of the beam diagnostic system.
Combined with the with beam diagnostic and particle transport numerical simulation code FLUKA results radiation dose measurement enables one to calculate experimental sample irradiation parameters for several
materials science and biological experiments that are being conducted on AREAL facility.

AREAL radiation safety

Along with RF gun two acceleration structures will permit to reach electron beam energy 20 MeV. Laser driven photo gun capability limits beam current by 0.2 nA for both single and multi-bunch modes of the LINAC operation. Strait beam line is planned, without beam compressors and beam turns, making beam dump at the end opposite the sole source of the secondary neutron and gamma radiation that safety system should cope with.

Table 1: LINAC parameters relevant to radiation safety.

Bunch charge	200 pC
Electron energy at the gun exit	5 MeV
Electron final energy	20 MeV
Beam current	0.2 nA
Beam final mean power	4 mW
Beam distance from the wall	1.5 m
Beam distance from the ceiling	2.2 m

Radiation by electrons: The major radiation loss components of the 20 MeV electrons are:

- Giant-Resonance-Neutrons: Those neutrons with energy range between 0.1MeV and 20MeV are produced by the bremsstrahlung photons in the core of the electromagnetic shower.
- Direct Gamma: Photons with energies between 0.1MeV and 20MeV leaving the shower core.

High-energy electrons predominantly lose energy in matter by bremsstrahlung, and high-energy photons by e+ e− pair production. The characteristic amount of matter traversed for these related interactions is called the radiation length R_l, usually measured in [g/cm^2]. It is both the mean distance over which a high-energy electron loses all but 1/e of its enerAgy by bremsstrahlung, and 7/9 of the mean free path for pair production by a high-energy photon. It is also the scale length for describing high-energy electromagnetic cascades.

The radiation length for a given material consisting of a single type of nuclei can be approximated (compact fit to the data) by the following expression [1]:

$$R_l = \frac{716A}{Z(Z+1)\ln(287/\sqrt{Z})}[g/cm^2], \quad (1)$$

where A is the atomic mass and Z is the atomic number of the absorber nucleus.

For electrons at lower energies (below few tens of MeVs), the energy loss by ionization is predominant. An electron loses energy by bremsstrahlung at a rate nearly proportional to its energy, while the ionization loss rate varies only logarithmically with the electron energy. The critical energy E_c is sometimes defined as the energy at which the two loss rates are equal [1]. The value of the critical energy when bremsstahlung starts to prevail over ionization mechanism can be obtained by the expressions

$$E_c = \frac{610MeV}{Z+1.24} \quad (2)$$

for solids and liquids.

The Molière radius is a characteristic constant of a material giving the scale of the transverse dimension of the fully contained electromagnetic showers initiated by an incident high energy electron or photon. By definition, it is the radius of a cylinder containing on average 90% of the shower's energy deposition. It is related to the radiation length R_l by the following approximate formula:

$$R_M = 0.0265R_l(Z+1.2), \quad (3)$$

where Z is the atomic number.

Beam Dump; Standard-Target: Dose and shielding calculations presented are based on the algorithms and formulae borrowed from SHIELD11 computer code [2].

Electron beam will be terminated by beam dump target, which is iron cylinder surrounded by shielding. The parameters of the some common beam target materials are presented in table2. Electron radiation losses critical energy for the iron is 22.4 MeV (Formula 2). That means about half of their initial energy 20 MeV electrons will loss through bremsstrahlung, while the ionization mechanism is account for the rest.

Empiric formulae used by SHIELD11 code are derived on the basis of the numerous measurements and particle tracking simulations are applied for the standard target [2]. Standard-target is 12-inc long iron cylinder with 2-inc radius. Those dimensions correspond to 17.3 radiation length and 3.74 Moliere radii.

Secondary neutron and gamma radiation will be produced also when beam electrons scrap beam pipe inner surface or hit pieces of the beam diagnostic equipment. However, since no bunch compressors and beam turns are foreseen the main concern in terms of secondary radiation remains beam dump.

Table 2: Material parameters for concrete, iron and lead built in and used in SHIELD11, effective atomic number: Z, atomic mass: A, density: ρ [g/cm^3], radiation length: R_l [g/cm2], Moliere radius R_M: [g/cm2].

	Concrete	Iron	Lead
Z	13	26	82
A [g/mole]	26.98	55.85	207.19
ρ [g/cm^3]	2.35	7.87	11.35
R_l [g/cm^2], ([cm])	26.7, (11.36)	13.84, (1.76)	6.37, (0.561)
R_M [g/cm^2], ([cm])	11.1, (4.72)	10.7, (1.36)	14.2, (1.25)
E_c [MeV]	42.8	22.4	7.33

Giant-Resonance-Neutrons: Giant-Resonance-Neutrons are emitted nearly isotropically in angle. Neutrons yield per unit power loss is proportional to the beam energy and depends on the target material as $Y = 0.121Z^{0.662}$, where Yield is expressed in the units [10^{12} n/s/kW] .To obtain dose at 1cm distance from the source one should multiple it by the factor 3.2×10^{-10} Sv-cm^2/n:

$D_{ne} = 4.93Z^{0.662}(E\times10^{-16})$ [Sv/e],where E is the beam energy in MeV. For the beam energy 20 MeV and current 0.2 nA one gets neutron dose rate at dump target

$$D_n = 1.775Z^{0.662}\frac{EI}{q_e}\times10^{-13} = 0.3835 \text{ Sv/h.} \quad (4)$$

Direct Gamma: The angular and energy distribution of the gamma radiation emitted directly in shower core at radiation source can be expressed by the following formula [2]:

$$D_\gamma = (\frac{EI}{q_e})(3..031Ee^{-0.959\sqrt{\vartheta}}\times10^{-13} + 7.5e^{-\vartheta/72.2}\times10^{-8}), \quad (5)$$

where D_γ is the gamma dose rate at the radiation source in the units of [Sv/h], E is the beam energy in [MeV]s and ϑ is radiation angle in degrees with respect to beam direction. Putting in $E = 20$ MeV and $\vartheta = 90$ degrees one gets $D_\gamma = 0.5378$ Sv/h. The first term in formula (5) describes radiation emitted in forward direction $(\vartheta = 0^\circ - 5^\circ)$, while second term describes lateral and backward radiation. Angular and energy dependence of the direct gamma radiation dose rate near target is illustrated in Fig. 1.

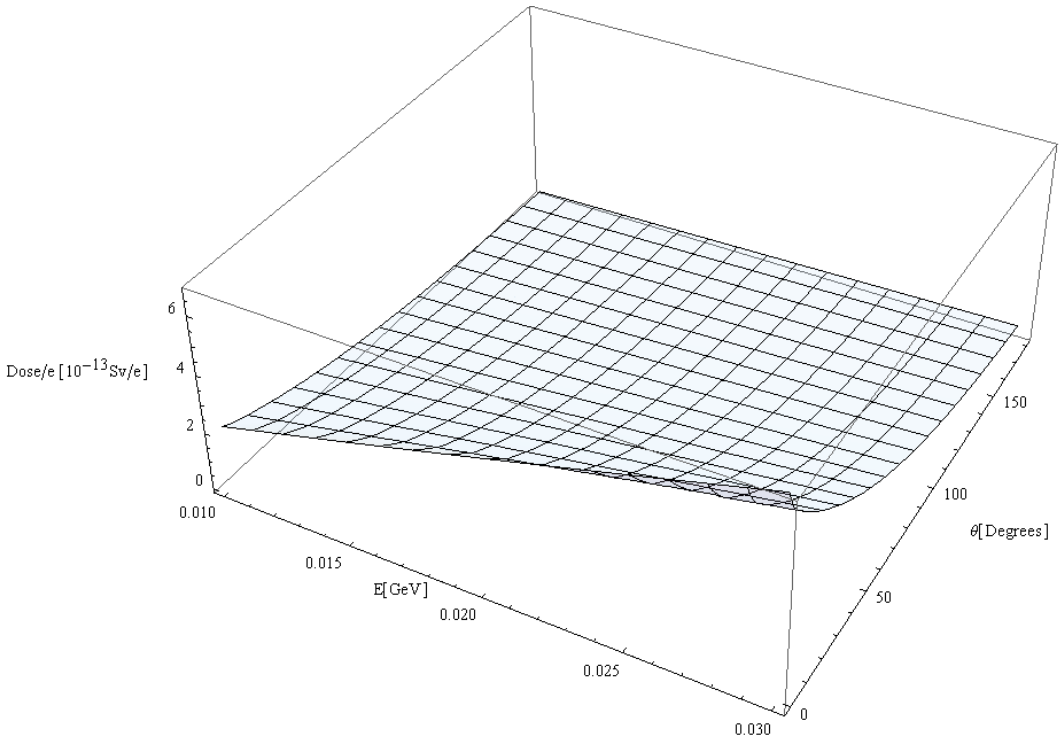

Figure1: Direct gamma radiation dose per electron at standard target. Maximum of radiation lays in forward direction and increases with electron energy nearly linearly.

Shielding: The shielding has to be dimensioned to keep the ambient dose equivalent rate below the limit of 0.125 μ Sv/h (the sum of both, the neutron- and γ-dose rates) [3]. The parameters of the some common shielding materials are given in the Table 3. The mean free path λ [g/cm^2] is the parameter that defines materials ability to absorb radiation $F = F_0 e^{-\lambda / d}$, where F is the fluence and d [g/cm^2] is the material thickness. Neutrons are effectively being absorbed by concrete, since it contains hydrogen (in bounded water molecules). For the attenuation of the gamma radiation high Z materials (like Led) are being applied (Formulae 1-3 and Table 3).

Table 3: Removal free path for some shielding materials

	Concrete	Fe	Pb
ρ [g/cm^3]	2.35	7.87	11.35
Neutrons [g/cm2], ([cm])	30, (12.8)	47, (5.97)	97, (8.55)
Gamma [g/cm2], ([cm])	42, (17.9)	33.6 (4.27)	24, (2.11)

Tunnel walls: The distance between the strait beam pipe and the tunnel nearest wall will be 150 cm. Air gap will reduce dose rate outside tunnel significantly, since both neutron and gamma lateral radiation are isotropic decrease proportionally to the $\sim 1/L^2$, where L is the distance from the source. Thick concrete walls screen the area outside from the radiation emitted not only at beam dump target but also from the radiation produced when beam hit the pieces of vacuum chamber, slit walls, etc. To ensure $0.125 \mu Sv/h$ ambient dose 90cm total width of concrete shielding is necessary (Fig.2). Introducing only 10 cm Led additional shielding decreases necessary concrete thickness to 50 cm (Fig. 3).

Beam dump shielding

The beam dump will consist of iron core with lateral and downstream shielding. Iron target be 30 cm long cylinder with 5 cm thickness. 10 cm Led shields will surround iron core (laterally and downstream). 50 cm thick concrete block will compose outer shielding of the beam dump.

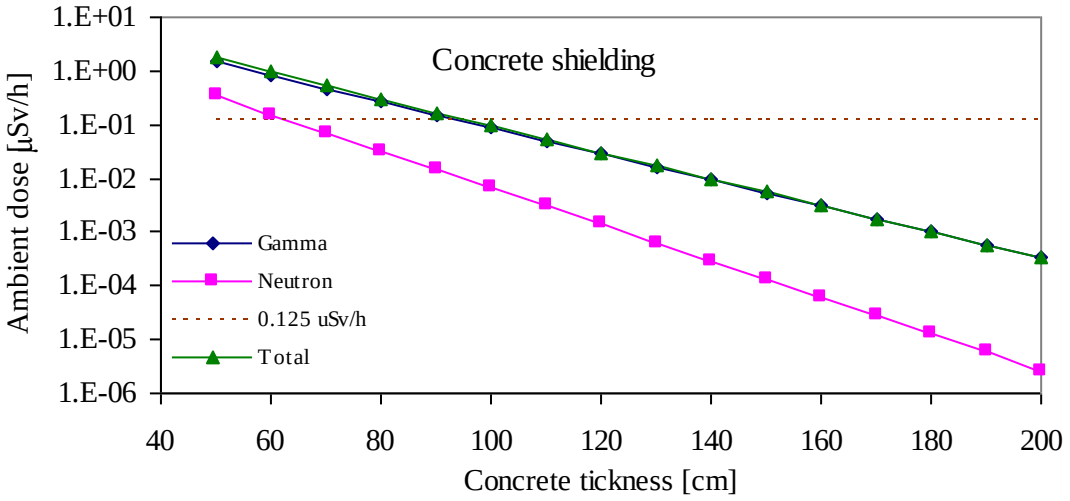

Figure 2: Ambient dose outside tunnel vs. concrete wall thickness. Dotted line shows target level of equivalent dose- $0.125 \mu Sv/h$.

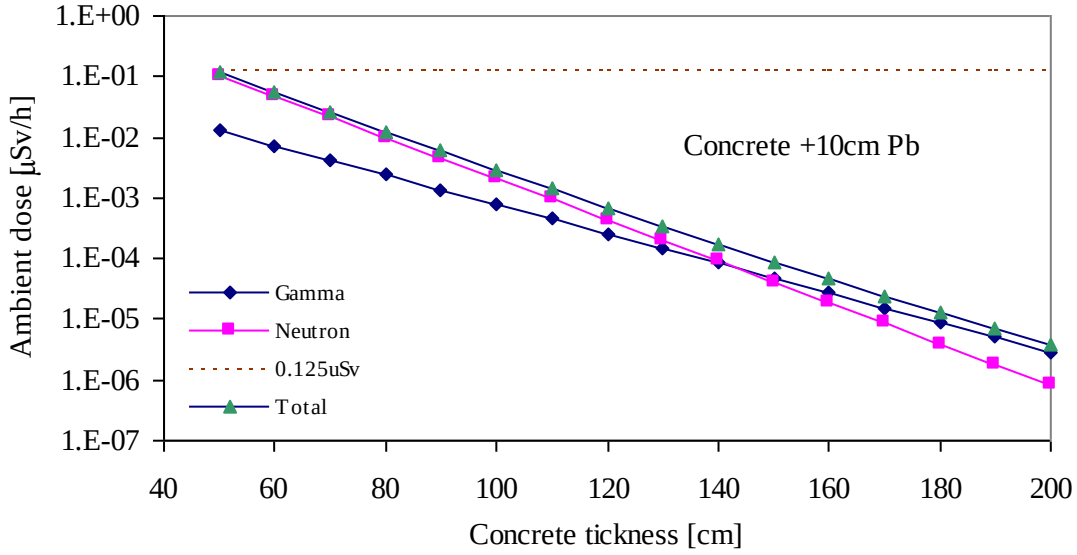

Figure 3: Ambient dose outside tunnel vs. concrete wall thickness. Dotted line shows target level of equivalent dose: $0.125 \mu Sv/h$. Additional 10cm Led shielding around beam dump target effectively reduces gamma dose.

EQUIPMENT

Gamma-scout dosimeter

Geiger-Muller counter tube based alpha, beta gamma radiation meter GAMMA_SCOUT with data reading and display software

Display: Liquid-crystal display (LCD), 4-digit, numeric with description,
quasi-analogue logarithmic bar chart,
Operating mode indicators
Radiation Detector: End-window counting tube to the Geiger-Müller principle
Stainless steel housing,
Measuring length 38.1 mm, measuring diameter 9.1 mm,
Mica window 1.5 to 2 mg/cm2
Zero rate <10 pulses per minute with screening by 3mm AI and 50 mm Pb,
operating temperature -20 to +60°C,
operating voltage approx. 450 V calibrated scale 0.01 µSv/h to 5,000.00 µSv/h
Radiation Types: α from 4 MeV
β from 0.2 MeV
γ from 30 keV
Selection shield: $\alpha + \beta + \gamma$ without shielding
$\alpha + \beta$ AI foil approx. 0.1 mm, shields a completely
γ Al shield approx. 3 mm, shields α completely and β to 2 MeV, weakens γ by less than 7% based on Cs-137
Power Consumption: Less than 10 microamperes under environmental radiation
Memory: 256,000 byte (100,000 data sets)
Housing: Impact-resistant plastic
Dimensions: Length 163 mm x width 72 mm x height 30 mm.

Ionization chamber based radiation area survey meter STEP OD-01 with software

Measuring value: Ambient dose equivalent H*(10),
Ambient dose rate equivalent dH*(10)/dt,
Directional dose equivalent H'(0.07, Ω),
Directional dose equivalent dH'(0.07, Ω)/dt,
Type of radiation: Photon and beta radiation
Mixed radiation fields
Pulsed radiation fields
Display ranges:
Dose rate 0 µSv/h .. 2000 mSv/h
Dose 0 .. 2000 µSv
Energy range:
Photon energy 6 keV to 7.5 MeV (15 MeV)*(1)*
Beta energy 60 keV to 2 MeV
Radiation direction referred to ± 45° for H'(0,07)
preferential direction (axial) ± 90° for H*(10)
Detector type: Air-opened ionisation chamber,
Volume 600 cm³,
PMMA-Shielding disposable, 550 mg/cm²
Face sided entry window 3.3 mg/cm² (metal covered PETP foil)
Preferential direction/point of reference axial, marked on detector
Wall potential + 400 V (µSv, mSv/h)+ 40 V (µSv/h)
Measurement uncertainties:
Linearity < 15 % (fine measurement range 20) ± 10 % (fine measurement ranges 200 and 2000)

Warm-up time: 2 minutes
Power Supply: Batteries, Accumulators
Current consumption approx. 30 mA @ 6 V
Battery lifetime approx. 100 h
Display unit: 31/2 – digit LC-display, back lighted
Digit height: 12 mm
Additional bar display
Automatic switch for fine measurement range decades
Air pressure: 80 to 110 kPa
Relative humidity: max. 80 %

Gamma-scout dosimeter, general view

STEP OD-01 survey meter

Calculation and simulation software: FLUKA, SHIELD11, MATHLAB MATEMATICA, MS EXCEL.

ABSORBED DOSE CHARACTERISTICS FOR IRRADIATION EXPERIMENTS AT AREAL 5 MEV ELECTRON LINAC

Existing electron photogun facility at the CADLE SRI currently can provide electron beam with the energy up to 5 MeV. The beam is being used as an irradiation source in the number of material science and life science experiments [5]. Performed beam particle tracking simulations along with intensive application of the beam diagnostic instruments (bending magnet, YAG stations, Faraday cups) allow control of the experimental samples' irradiation parameters, particularly exposure times for given dose as well as absorbed dose spatial distribution.

Electron beam parameters and absorbed dose

AREAL electron linac can produce clean and controllable 2-5 MeV electron beam with 30-250 pC pulse charge and 1- 20 Hz repetition rate [6]. The main parameters of the electron beam are can be monitored and manipulated to apply precise irradiation dose for the experimental sample. AREAL uses photogun driven by 0.45 ps laser pulses thus conditioning short bunch duration taking into account that RF wavelength is 0.1 m. Main parameters of the AREAL electron beam are presented in Table 1.

Table 1: AREAL Beam Parameters

Energy	2–5 MeV
Pulse charge	30–250 pC
Pulse length	0.45 ps
Norm. emittance	≤ 0.5 mm-mrad
RMS energy spread	≤1.5 %
Pulse repetition rate	1-20 Hz
RF frequency	3 GHz

Following the recommendations of the International Commission on Radiation Units and Measurements (ICRU) one can find out absorbed dose from electrons by the formula $D = \varphi\left(S/\rho\right)_{col}$, where φ is electrons fluence (in 1/cm^2 units) and $\left(S/\rho\right)_{col}$ (in MeV cm^2/g units) is the mass collision stopping power, resulting from electron interactions with the orbital electrons in atoms [4,7]. The resulting formula for the absorbed dose rate will be:

$$\dot{D}\left[\frac{Gy}{s}\right] = \frac{Q[pC]\cdot n[Hz]}{e[C]\cdot A[\mathrm{cm}^2]} \times \left(\frac{S}{\rho}\right)_{col}\left[\frac{MeV\cdot cm^2}{g}\right] \times 10^{-3}.$$

Here $Q[pC]$ is the pulse charge in picocoulombs, $n[Hz]$ is repetition rate $e[C]$ is electron charge and $A[\mathrm{cm}^2]$ is beam spot size area at the sample surface. Since particles distributions are nearly Gaussian both in transverse vertical and horizontal directions A can be calculated as the area limited by ellipse $A = \frac{\pi}{4}XY$, where X and $Y$are beam spot sizes (FWHM) in horizontal and vertical directions.

Beam parameters measurements

Advanced Research Electron Accelerator Laboratory (AREAL) based on photo cathode RF gun has been constructed at CANDLE.

The AREAL RF photogun experimental operation provides the electron bunches with up to 4.8 MeV energy and 5 nC mean current. The gun section contains the focusing solenoid, magnetic spectrometer, horizontal/vertical corrector magnet, Faraday Cups (FC) and YAG screens with cameras. The charge of individual bunches was measured using two FCs.

The beam energy and the energy spread measurements have been performed using the magnetic spectrometer located downstream the gun focusing solenoid. The spectrometer consists of 90° bending dipole magnet and the YAG screen station. The beam absolute energy is determined by measuring the beam position on the YAG screen with respect to the central trajectory position, which was calibrated with particle tracking simulations using the measured dipole magnetic field distribution. The energy spread is evaluated using the beam horizontal profile on the YAG screen. The horizontal width of the distribution is determined by the width of the energy distribution.

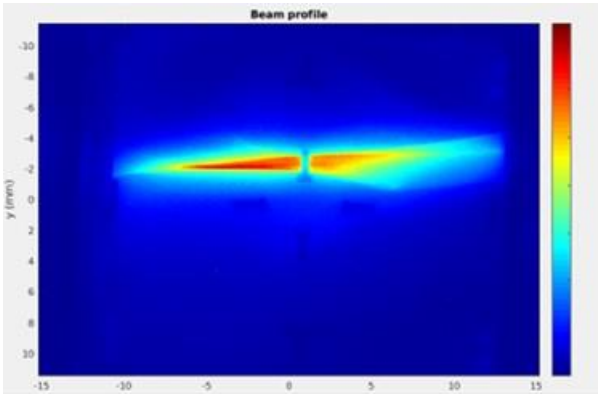

Figure 1: Electron beam image on the YAG screen.

Dedicated software has been created at CANDLE that allows digital processing of the YAG screen image of the AREAL beam and to derive digital values of the beam particles transverse distributions parameters. Fig. 1. presents the 250 pC charge beam profile at the YAG screen in the bended beam (dipole magnet is switched on) section. The corresponding beam energy is about 4.2 MeV and the energy spread is below 1.5%. Beam transverse profile measurements results have been used to calculate absorbed dose spatial distribution. The particles energy spread is dominated by an uncorrelated contribution, which is decreasing with acceleration being inversely proportional to beam energy. Compact sized experimental samples have been irradiated by 2 - 4.8 MeV electron beam at the AREALThe samples were exposed to the beam at a distance 3 cm from the exit port. At those positions typical beam spot sizes were 15 mm in diameter for strait beam and 15 m. m × 35 mm for bended one. For radiation biology experiments the objects of the larger size have been used by positioning them in 40 cm distance from the beam exit window.

Beam profiles have been visualized and quantities of particles distributions were being estimated using YAG screen stations both in strait and bended beam sections.

For the beam charge measurement beam has been focused on the FC entrance window by manipulating the solenoid magnets current. Thus routinely 250 pC charge was being measured for the strait beam (see Fig. 2) and at least 30 pC value has been obtained for the bended beam.

While pulse charge is being measured by FC permanently, finding out the beam spot sizes at experimental sample position is not trivial. For the later purpose thin glass plates are being irradiated by electron beam at the experimental sample frontal position for 30 minutes. Obtained image is gradually faded within a few days, however allows estimation of the beam spot sizes (Fig. 3.). The image is permanent one if quartz is used instead of ordinary glass.

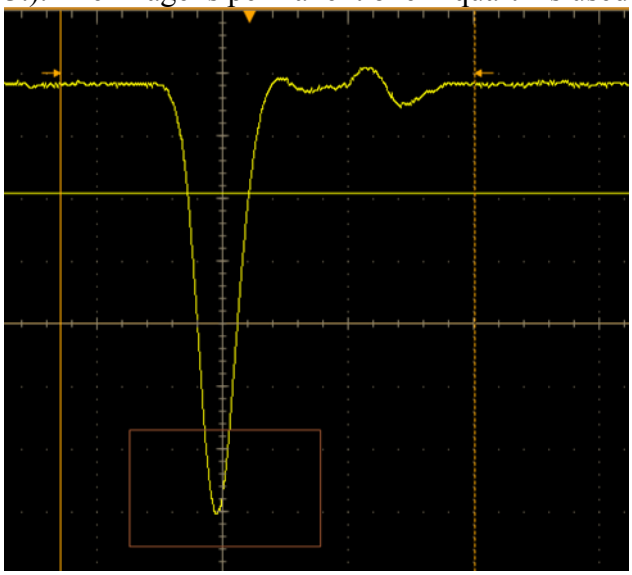

Figure 2: Signal from FC for the bent beam.

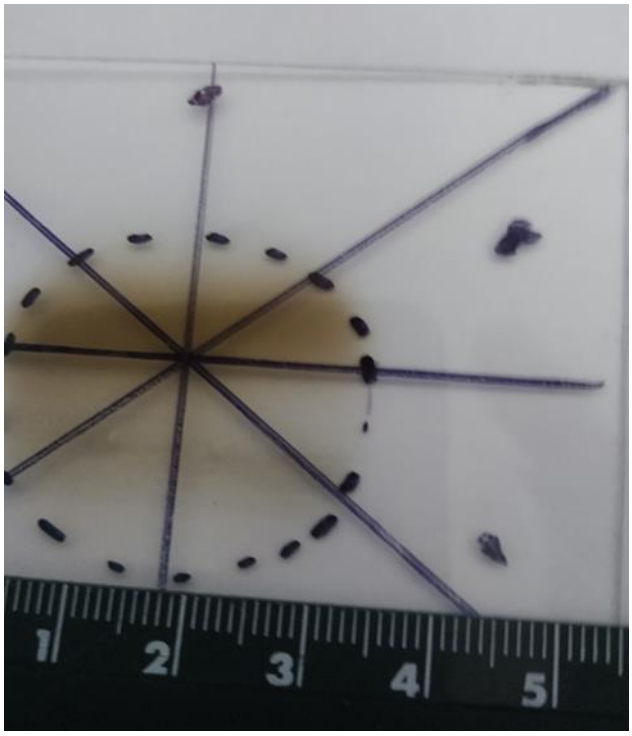

Figure 3: Electron beam image on glass plate (bent beam) at sample location.

Numerical simulation with FLUKA

Measured beam parameters along with experimental sample geometry, position and material composition data enables one to estimate absorbed dose. More accurate definition of the absorbed dose and its distribution in the volume of the irradiated material can be obtained with numerical modelling.

Absorbed dose in the sample through the electron has been calculated using the particle transport simulation modelling code FLUKA [2]. Digital simulations to take into account accurately the beam scattering within the vacuum window material (Titanium) and in the air. The results of beam parameters measurements used for simulations include:

- Beam current measurements by Faraday cup;
- Beam transverse profile imaging by YAG screen and camera station;
- Focusing solenoid magnet current adjustment and definition of the beam minimal spot sizes;
- Beam energy and energy spread measurement by spectrometer consisting of dipole magnet and YAG screen system.

The processing of the YAG screen image reveals that the beam has Gaussian distribution of electrons along horizontal and vertical directions, i.e., perpendicular to the beam direction. Default function of FLUKA does not let one to simulate the beam with required parameters. Default function is designed to calculate physical quantity per electron that gives only integral values of absorbed dose. Therefore, a custom user routine was programed in FORTRAN language. The program is able to generate beam with the parameters and distributions that actually available at AREAL linear accelerator. Digital simulations extended to take into account accurately the beam scattering within the vacuum window material (Titanium) and within the air.

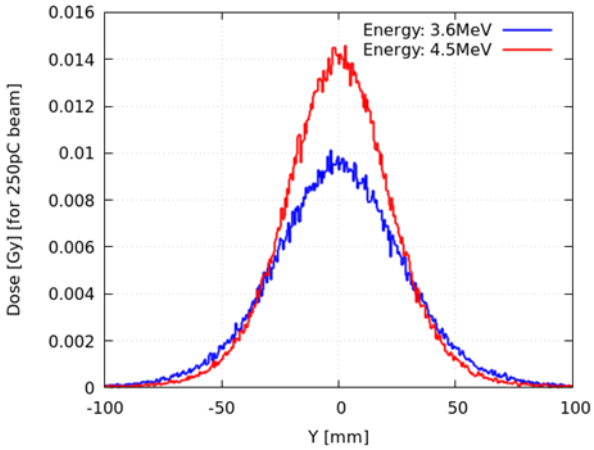

Figure 4: Dose distribution along vertical axis. Distributions are normalized per 250 pC.

Figure 4 and Fig. 5 show the results of the FLUKA simulations of the beam interaction with the biological sample model (water filled cylinder with 5 cm diameter and 20 cm height) positioned at 40 cm distance from the vacuum window vertical to beam propagation direction. Note, that the origin of the coordinate system coincides with the geometrical centrum of the cylinder. Dose distributions become narrower and shift deeper within the volume of the experimental sample with the increase of the impact beam energy. Note, that in Continuous Slowdown Approximation (CSDA) model electron range in the water is 2.0 cm for 3.6 MeV energy and 2.5 cm for 4.5 MeV energy [7].

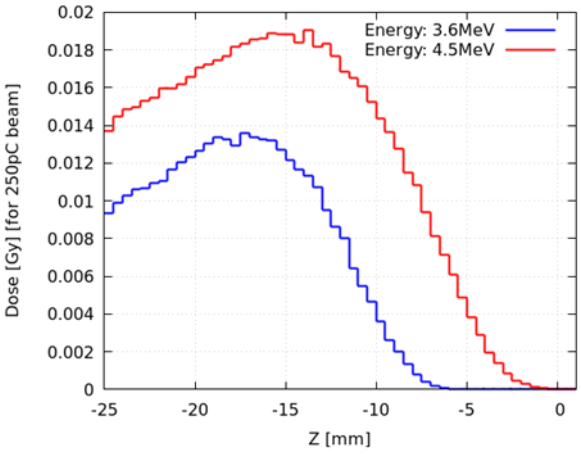

Figure 5: Dose distribution along Z axis, pointing to beam propagation direction. Distributions are normalized per 250 pC.

Conclusion

FLUKA simulations have been performed aimed at calculation of the required exposure time to provide necessary irradiation dose for the given beam parameters (energy, current, spatial sizes and divergence).

Input parameters for FLUKA simulations of the electron beam interaction with experimental sample have been defined relying on two sets of the data. Beam parameters measurements results have been combined with the sample geometrical and composition parameters allowing calculation of the absorbed dose within the experimental sample volume. However, digital modelling by Monte Carlo particle transport code proved to be more instrumental method for precise definition of the absorbed dose and its distribution within the experimental sample volume.

PRACTICAL HOURS

The

The main task: Calculation of the absorbed dose within the experimental sample by AREAL accelerator electron beam

Following the recommendations of the International Commission on Radiation Units and Measurements (ICRU) one can find out absorbed dose from electrons by the formula $D = \varphi\left(S/\rho\right)_{col}$, where φ is electrons fluence (in 1/cm^2 units) and $\left(S/\rho\right)_{col}$ (in MeV cm^2/g units) is the mass collision stopping power, resulting from electron interactions with the orbital electrons in atoms .The resulting formula for the absorbed dose rate will be:

$$\dot{D}\left[\frac{Gy}{s}\right] = \frac{Q[pC]\cdot n[Hz]}{e[C]\cdot A[\mathrm{cm}^2]} \times \left(\frac{S}{\rho}\right)_{col}\left[\frac{MeV\cdot cm^2}{g}\right] \times 10^{-3}.$$

Here $Q[pC]$ is the pulse charge in picocoulombs, $n[Hz]$ is repetition rate ,$e[C]$ is electron charge and $A[\mathrm{cm}^2]$ is beam spot area at the sample surface. Since particles distributions are nearly Gaussian both in transverse vertical and horizontal directions A can be calculated as the area limited by ellipse $A = \frac{\pi}{4}XY$, where $X\ and\ Y$are beam spot sizes (FWHM) in horizontal and vertical directions.

Task1: The measurements of the background dose rates in AREAL machine hall and neighboring premises using Geiger-Muller counter and Ionization chamber survey meter;
In measuring mode of the GAMMA_SCOUT dosimeter (press the corresponding button), the display shows the current radiation measurement reading every 2 sec. GAMMA-SCOUT stores all registered pulses in its internal memory and keeps them ready for you to use when desired. Stored data in the memory can be read out and processed using GAMMA_SCOUT TOOLBOX software. Use mini USB cable to connect the dosimeter with the PC USB port and transfer the measurement data to computer for visualization and processing.
Prior to measurement the zero of the STEP OD-01 device should be verified. Electrical zero can be considered as balanced, if display indicates the value in the range of $0 \leq 0.05$. The meter switch must be set at the measuring range μSv. Note that after switching between the ranges it takes about 2min before internal circuit come to balance and the device is ready for the measurements. Use provided USB cable to connect the dosimeter to the PC, run dedicated software (that should be installed on PC) for the reading out, visualization and processing of the measurement data. Try to interpolate some possible discrepancy between the data obtained by two principally different type of dosimeters relying on the differences of the technical characteristics (energy ranges, sensitivities, etc.).

Task 2: Search for Radon concentration high levels in the basement rooms applying GAMMA_SCOUT dosimeter;
Survey the basements rooms using GAMMA_SCOUT dosimeter with the Geiger-Muller counter . Measure the background dose at several fixed positions with counter window open (put the switch on the position $\alpha + \beta + \gamma$), then turn the switch to the position $\beta + \gamma$ thus preventing α particles to reach the counter window and repeat the measurement. The duration of the single measurement should be at least 2 minutes to gather some statistics. If the measured dose value in first regime is significantly higher than that in the second regime, it can be interpreted us the clear indication of higher level of Radon concentration. Note that the dosimeter is sensitive to α particles with the energy more than 4 MeV and α particles from the Radon decay chain have the energy 5.49 MeV, 6 MeV, 7.69 MeV, etc. Dosimeter displays the results starting 10 counts per minute.

For the absolute measurement of the Radon concentration elaborate techniques should be applied and that problem is beyond the scope of the current work.

Task 3: Perform measurements of the dose rates during the AREAL accelerator operation by ionization chamber at several fixed positions in the machine hall and comparison with the FLUKA simulation results. A protection barrier/wall with single and then with two layer of concrete bricks should be assembled between beam target and dosimeter to demonstrate radiation protection by increased shielding.

Task 4: For the radiation loss study of AREAL beam at the target with various materials and the different thickness measurement of the dose rate dependence on the beam current measured by Faraday Cap should be conducted. It is anticipated to use several 0.5 mm tick Al sheets and 1cm 2cm long water filled polyethylene containers as targets.

Task 5: Experimental study of the dose rate dependence on the beam energy measured in dispersion section using bending magnet and YAG screen station (Note that absorbed dose is nearly independent of beam energy in the 2- 5 MeV region).

Remarks:
After detailed discussion of the course it was suggested to use a beam diaphragm to center the beam by minimizing the beam losses; compare the result of this attempt with the beam profile team in terms of their result on the beam size; compare results of measurement of background dose rates in AREAL machine hall and environment; search for Radon concentration in the basement rooms; compare measurements with FLUKA simulation results; demonstrate radiation protection by increased shielding.
Add the radiation loss study of AREAL beam at the target with various materials and the different thickness.

LITERATURE

[1] M. Tanabashi et al. (Particle Data Group), Phys. Rev. D 98, 030001 (2018). (http://pdg.lbl.gov).
[2] http://www.fluka.org/.
[3] W.R. Nelson, The SHIELD11 Computer Code, T.M. Jenkins, SLAC-R-737, UC-414.
[4] International Commission on Radiation Units and Measurements, Fundamental Quantities and Units for Ionizing Radiation, ICRU Report 60 (1998).
[5] V. M. Tsakanov, et al., "AREAL Low Energy Electron Beam Applications in Life and Materials Sciences", Nuclear Instruments and Methods in Physics Research A, v.829, pp. 248-253, 2016.
[6] B. Grigoryan, et al., "Status of AREAL RF Photogun Test Facility" Proceedings of IPAC2014, pp., 620-623, Dresden, Germany 2014.
[7] INTERNATIONAL COMMISSION ON RADIATION UNITS AND MEASUREMENTS, Stopping Powers for Electrons and Positrons, Rep. 37, ICRU, Bethesda, MD (1984).

APENDIX A

Radiological quantities and units [1]

Physical quantities

The **fluence** (unit: $1/m^2$) is the number of particles incident upon a small spheric cross-sectional area
It can be shown that the fluence is given by the sum of the particle trajectory lengths in the volume unit volume .

The **Absorbed dose**, (unit: gray, 1 Gy=1 J/kg=100 rad) is the energy deposited by ionizing radiation in a volume element of a material divided by the mass of this volume element.

The **linear energy transfer, L or LET** (unit: J/m, often given in keV/ μ m)is the mean energy, lost by a charged particle in traversing a unit distance in matter. ***Low*-LET *radiation***: x rays and gamma rays or light charged particles such as electrons that produce sparse ionizing events at a molecular scale (L < 10 keV/ μ m).
High*-LET *radiation: neutrons and heavy charged particles that produce ionizing events densely spaced at a molecular scale (L > 10 keV/ μ m).

Protection quantities

Protection quantities are dose quantities that quantify the extent of exposure of the human body to ionizing radiation.

The **equivalent dose** (unit: sievert, 1 Sv=100 rem) in an organ or tissue is equal to the sum of the absorbed doses in the organ or tissue caused by different radiation types weighted with radiation weighting factors. It expresses long-term risks (primarily cancer and leukemia) from low-level chronic exposure. The values for wR recommended by ICRP [6] are given in Table 1.

Table 1: Radiation weighting factors, wR.

Photons, electrons and muons	1
Neutrons, En < 1 MeV	$2.5+ 18.2 . \exp[-(\ln En)^2/6]$
Neutrons, 1 MeV $\leq En \leq$ 50 MeV	$5.0+ 17.0 . \exp[-(\ln(2En))^2/6]$

The **effective dose**, (unit: sievert) is the sum of the equivalent doses, weighted by the tissue weighting factors of several organs and tissues of the body that are considered to be most sensitive [7].

Operational quantities

The **operational quantities** are used for the assessment of effective dose or mean equivalent doses in tissues or organs, since protection quantities are not measurable in practice.

Ambient dose equivalent, (unit: sievert): The dose equivalent at a point in a radiation field that would be produced by the corresponding expanded and aligned field in a 30 cm diameter sphere of unit density tissue (ICRU sphere) at a depth of 10 mm on the radius vector opposing the direction of the aligned field. Ambient dose equivalent is the operational quantity for area monitoring.

Personal dose equivalent, (unit: sievert): The dose equivalent in ICRU tissue at an appropriate depth, below a specified point on the human body. The specified point is normally taken to be where the individual dosimeter is worn. For the assessment of effective dose, with a depth 10 mm is chosen, and for the assessment of the dose to the skin and to the hands and feet the personal dose equivalent, with a depth 0.07 mm, is used. Personal dose equivalent is the operational quantity for individual monitoring.

APENDIX B
Background radiation sources

The worldwide average of the annual whole-body dose equivalent due to all sources of **natural background radiation** ranges from 1.0 to 13 mSv with an annual average of 2.4 mSv (that corresponds to the rate of 0.27 μSv/h) [1]. In certain areas values of 50 mSv have been measured. Typically more than 50% originate from inhaled natural radioactivity, mostly radon and radon daughters. Dose equivalent rates due to **cosmic ray background radiation** range from less than 0.1 μSv/h at sea level to a few μSv/h at aircraft altitudes. Artificial sources (medical, cigarettes, air travel, building materials, etc.) contribute 0.61 mSv.
Background radiation main sources are shown in table. These classification can be retrived from the two following documents.:
a) United Nations Scientific Committee on the Effects of Atomic Radiation (2008 (published 2010)). *Sources and effects of ionizing radiation*. New York: United Nations. p. 4.
b) *Ionizing radiation exposure of the population of the United States*. Bethesda, Md.: National Council on Radiation Protection and Measurements. 2009.

Radiation source	World	USA	Remark
Inhalation of air	1.26	2.28	mainly from radon, depends on indoor accumulation
Ingestion of food & water	0.29	0.28	(K-40, C-14, etc.)
Terrestrial radiation from ground	0.48	0.21	depends on soil and building material
Cosmic radiation from space	0.39	0.33	depends on altitude
sub total (natural)	2.40	3.10	sizeable population groups receive 10-20 mSv
Medical	0.60	3.00	world-wide figure excludes radiotherapy; US figure is mostly CT scans and nuclear medicine.
Consumer items	-	0.13	cigarettes, air travel, building materials, etc.
sub total (artificial)	0.61	3.14	
Total	3.01	6.24	**millisievert per year**

APENDIX C

Occupational exposure

The ICRP recommends limiting occupational radiation exposure to 50 mSv per year, and 100 mSv in 5 years [1]. In 2002 IAEA recommended that occupational doses below 1–2 mSv per year do not warrant regulatory scrutiny[1]. The limit in the EU-countries and Switzerland is 20 mSv per year, in the U.S. it is 50 mSv per year. The effective dose limit for general public is typically 1 mSv/year.